CHAPTER 4

GAIN AND BANDWIDTH IMPROVEMENT STUDIES OF MILLIMETER WAVE GYRO-TWYSTRON AMPLIFIER *

*Part of this work has been accepted as:

S. G. Yadav, Vangalla Veera Babu and M. Thottappan, "Gain and Bandwidth Improvement Studies of Millimeter Wave Periodically Dielectric Loaded Gyro-Twystron Amplifier" in *IEEE Transactions on Electron Devices*, doi: 10.1109/TED.2022.3217760.

4.1. Introduction

In Chapter 2 and chapter 3 the design and simulation study of unloaded gyro-twystron has been carried out, using the nonlinear theory and CST particle studio, respectively. The dispersion characteristics studies predicted the different spurious modes near by the operating TE_{01} mode. In the present chapter, the interaction structure of gyro-twystron is designed to suppress the spurious modes. Backward wave oscillations and instabilities of gyro-twystron are investigated using the linear theory and calculations are made to design oscillation tolerant structures and enhance the amplifier's gain and bandwidth.

The potential of a gyro-amplifier with a nonresonant interaction structure is suffered by an absolute instability and backward wave oscillations (BWOs) [152]. In gyro-twystron, the convective instability arises in the positive k_z region (Figure 4.3), near the cutoff frequency. With enough beam current, this convective instability transformed into absolute instability. The end reflections due to mismatch can also cause oscillations [152], [126]. The beam wave interaction inside the waveguide depends on the dispersion characteristics of the waveguide and this would be change if the waveguide dimensions are not uniform, and this property is used to change the dispersion characteristics according to the required applications. There are various waveguide shaping techniques are available that alter the characteristics of propagating or resonating structures, the antennas, and the electron beam devices. The various method of wave shaping are, vanes loading or ridges or the corrugation with waveguides [20]-[23], [43],[47], [88], [89], [140]-[150]. Corrugated horn antennas have applications as low-noise feeds for reflector antennas used in satellite communication, radio astronomy, radiometry, etc. [141]-[143]. A circular waveguide with azimuthally periodic vanes, referred to in literature as the magnetron-like structure, control the dispersion

characteristics and hence widen the bandwidth of the TWT [150],[151].The ooptimization of the disc parameters provides a control over the dispersion of the disc-loaded waveguide for wideband coalescence between the beam-mode and waveguide-mode dispersion characteristics and consequent wideband performance of a gyro-TWT [44]-[48].

In the present chapter, the distributed loss technique has been successfully introduced to control BWOs and their effects to maintain stability with a remarkable performance in gyrotron travelling wave amplifiers. There are multiple techniques, *i.e.* dielectric coated wall, slotted waveguide supported by dielectric, dielectric ring interstice with metal, to introduce distributed loss in gyrotron travelling wave amplifiers [90]. The present study is used the field and mode matching techniques for the analysis of a disc-loaded waveguide with reference to various modes [42]-[44], [153],[158].

At the University of California, McDermott *et al.* have used an aquadag coating on the waveguide wall to introduce losses in the interaction region and obtained ~140 kW power with 5% bandwidth at 92 GHz [154]. In 1994, Song *et al*. experimentally tested a 94 GHz gyro-TWT for high-resolution radar application operating in TE_{01} mode with unity pitch, which had delivered ~59 kW saturated power with ~42 dB gain and efficiency of ~27 % [155]. Chao Hai Du *et al*. have studied the instability in a BeO-SiC supported waveguide structure and predicted ~68 kW of power and efficiency of ~32 % with 5% spread in electron beam [15]. Yan *et al.* have experimentally tested a W-band gyro-TWT and observed ~112 kW power with zero stable drive at 93.5 GHz and a saturated gain of ~70 dB [93]. Recently, Guo Liu *et. al.* performed an experiment on W-band dielectric loaded gyro -TWT, and reported the peak power ~ 160 kW with the efficiency of 16 %. The reported gain and bandwidth are 75 dB and 8.5 GHz respectively [163].

In the present chapter,

- The PDL technique is used to stabilize a W-band gyro-twystron against the spurious mode to enhance the amplifire's output performance. The analytical model of PDL waveguide for W-band gyro-twystron have been discussed.
- The criticals sub assembalies including MIG, SSD collector and output window has designed and simulated corrosponding to the required output and their performance behaviors, have been discussed.
- In last the overall conclusion is drawn based on the present study of W band dielectric-loaded gyro-twystron.

4.2. Theoretical Modeling of PDL Gyro-Twystron Amplifier

The spurious oscillations in the travelling wave output section due to the absolute instability plagued the gyro-twystron. There are different sources of oscillations in the travelling wave output section. The primary source is an extension of the beam wave synchronism point into the negative k_z region, where convective instability changes into absolute instability. The reflections due to the input and output port mismatch are also an additional source of oscillation. Such oscillations can be cut off using severe or distributed losses in the RF interaction circuit. Losses could be introduced directly with the dielectric material coating on the waveguide wall or by introducing the dielectric inside the waveguide slots [88],[90],[92]-[96], [155-168].

The schematic of the periodic dielectric-loaded (PDL) waveguide section is shown in Figure1, which consists of three regions, including region A ($0 < r < r_w$ and $0 \le z \le \infty$) is a vacuum area, region B ($r_w < \Delta r < r_0$ and $0 < z \le w$) consists of a dielectric loading portion, and region C ($r_w < r \le r_w + \Delta r$ and $w < z \le (L - w)$) is an outside metallic portion. The fields in each sub regions are define and applied the applicable boundary conditions

that leading the homogeneous linear equations in the matrix form. The vanishing determinant of which, as a condition of non-trivial solution, gave the dispersion relation of the structure [153].

The electromagnetic field propagating inside the dielectric-loaded structure can be evaluated by using Maxwell-Vlasov equation and Laplace transformation with specified boundary conditions. The electric and magnetic field behaviors inside the cylindrical system are given as [20],[21],[23]

$$\nabla^2 E_{\parallel} - \mu\varepsilon \frac{\partial^2 E_{\parallel}}{\partial t^2} = 0 \qquad [4.1]$$

$$\nabla^2 B_{\parallel} - \mu\varepsilon \frac{\partial^2 B_{\parallel}}{\partial t^2} = 0 \qquad [4.2]$$

where, $E_{\parallel}$ and $B_{\parallel}$ are the electric and magnetic field in the direction of propagation, respectively, μ and ε are the permeability and permittivity of a specific medium, respectively. The above wave equations (4.1) and (4.2) may be solved, with reference to a structure that enjoys a cylindrical symmetry, for field quantities in the various regions of the structure, supposedly axially periodic like a disc-loaded circular waveguide (Figure 4.1). The specified boundary conditions on the azimuthally symmetric mode $(\partial/\partial\theta = 0)$ in a cylindrical coordinate system result in continuous electric and magnetic field at the boundary of two different regions:

$$H_{\parallel}^{A} = H_{\parallel}^{B} \text{ and } E_{\Phi}^{A} = E_{\Phi}^{B} \text{ at } (0 < r < r_w,\ 0 < z \le w) \qquad [4.3]$$

$$H_{\parallel}^{A} = H_{\parallel}^{C} \text{ and } E_{\Phi}^{A} = E_{\Phi}^{C} \text{ at } (0 < r < r_w,\ (L-w) < z \le w) \qquad [4.4]$$

At the conductor interface, the tangential component of the electric field must vanish:

$$E_{\Phi}^{B} = 0 \text{ at } (r = r_w + \Delta r,\ 0 < z \le w) \qquad [4.5]$$

$$E_{\Phi}^{C} = 0 \text{ at } (r = r_0,\ w < z \le L) \qquad [4.6]$$

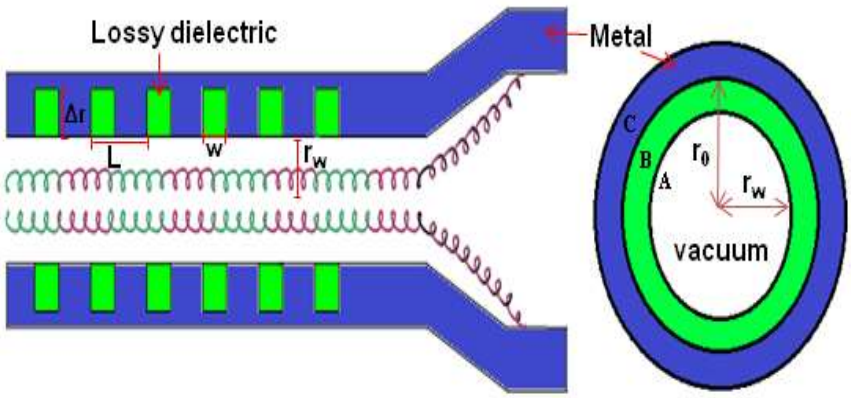

Figure 4. 1. Schematic diagram of PDL waveguide

The generalized fields in different regions of the PDL waveguide are analyzed using Flaquet theorem [168] accompanying with the sum of Bloch harmonics [155]-[159], [161]-[165]. The electric and magnetic fields for an azimuthally symmetric mode in region A are expressed as:

$$E_{\Phi}^{A} = \sum_{n=-\infty}^{\infty} \left(j\omega\mu_0 / \tau_n^A \right) F_n^A \left(\varsigma \right) X_0' \left(\tau_n^A \varsigma \right) e^{j(\omega t - k_n z)} \qquad [4.7]$$

$$H_{\parallel}^{A} = \sum_{n=-\infty}^{\infty} F_n^A \left(\varsigma \right) X_0 \left(\tau_n^A \varsigma \right) e^{j(\omega t - k_n z)} \qquad [4.8]$$

with radial propagation constant $\tau_n^A = \sqrt{\left((\omega/c)^2 - k_n^2 \right)}$, $k_n = k_0 + 2\pi n / L$ is the axial propagation constant, ς is the radius of the region A, F_n^A field constant in region A, n is the space harmonic, and X_0 and X_0' are the zero-order and first-order Bessel functions of the first kind, respectively. Similarly, the fields in region B are expressed as:

$$E_{\Phi}^{B} = \sum_{q=1}^{\infty} \left(j\omega\mu_0 / \tau_q^B \right) F_q^B \left(\varsigma \right) Z_0' \left(\tau_n^B \varsigma \right) e^{j\omega t} \sin\left(k_q z \right) \qquad [4.9]$$

$$H_{\parallel}^{B} = \sum_{q=1}^{\infty} F_q^B \left(\varsigma \right) Z_0 \left(\tau_n^B \varsigma \right) e^{j\omega t} \sin\left(k_q z \right) \qquad [4.10]$$

where, F_q^B is the field constant in region B,

$Z_0\left(\tau_q^B\varsigma\right)=X_0\left(\tau_q^B\varsigma\right)Y_0^{'}\left(\tau_q^B r_w\right)-X_0^{'}\left(\tau_q^B r_w\right)Y_0\left(\tau_q^B\varsigma\right)$ is the zero-order Bessel function and $Z_0^{'}\left(\tau_q^B\rho\right)$`first order Bessel function, $\tau_q^B=\sqrt{\left(\left(\varepsilon_0\varepsilon_r\omega/c\right)^2-k_n^2\right)}$ radial propagation constant in region B, $k_q=\left(q\pi/w\right)$ is the axial propagation constant and q is the modal harmonic number.

The boundary conditions discussed in equations (4.3) -(4.6) are applied to the field expressions of different regions expressed as equations (4.7) -(4.10) and yield the following eigenmode solutions of the PDL circular waveguide

$$\left[\frac{1}{\tau_n^A}\frac{X_0^1\left(\tau_n^A\varsigma\right)}{X_0\left(\tau_n^A\varsigma\right)}-\frac{1}{\tau_q^B}\frac{\varepsilon_B}{\varepsilon_A}\frac{Z_0^{'}\left(\tau_q^B\varsigma\right)}{Z_0\left(\tau_q^B\varsigma\right)}\right]\times\left[\frac{1}{\tau_n^A}\frac{X_0^{'}\left(\tau_n^A\varsigma\right)}{X_0\left(\tau_n^A\varsigma\right)}-\frac{1}{\tau_q^B}\frac{\mu_B}{\mu_A}\frac{Y_0^{'}\left(\tau_q^B\varsigma\right)}{Y_0\left(\tau_q^B\varsigma\right)}\right]-\left(\frac{1}{\left(\tau_n^A\right)^2}-\frac{1}{\left(\tau_q^B\right)^2}\right)=0 \qquad [4.11]$$

The determinantal dispersion relation (D), obtained from equation (4.11), is determined using the field matching technique that reduces the field constant by matching the field intensity components in distinct media with suitable boundary conditions [158], [164]. In general, the dispersion relation involves with the determinant of infinite-order ($n=0,\ \pm1,\ \pm2,\ ...,\ \pm\infty$, and $m=1,\ 2,\ 3,\ 4,\ 5,\ ...,\ \infty$), which should be truncated at a finite order for the desired converging solutions. For infinite number of model harmonic modes and space-harmonic modes [158], [161]- [164].

$$\det\left|D\right|=0 \qquad (-\infty<n<\infty,\ 1\le m<\infty)$$

Although the equation (12) is involving with an infinite matrix in principle, for the numerical calculation, the matrix D was truncated to some manageable size, say, V of model harmonic modes: $m=1,\ 2,\ 3,\ ...,\ V$ and the space-harmonic modes: $n=0,\ \pm1,\ \pm2,\ ...,\ \pm(V-1)/2$, where, $V\ge1$ is a natural number, depends on simultaneous equations in terms of the field constants. Typically, we use a 7×7 matrix with $-3\le m,n\le+3$, for a converging solution [158], [164].

The fluctuation in field amplitude that corresponds to space harmonics and model harmonics is shown in Figure4.2, for the vacuum region and the dielectric region, respectively. Figure4.2. (a) illustrates the peak amplitude at the fundamental harmonic (n), and as the number of space harmonics increases, the field within the vacuum gradually diminishes. The influence of the model harmonics is shown to have a decreasing amplitude with increasing model harmonic in Figure 4.2 (b), which indicates that higher model harmonic components experience attenuation in the dielectric region.

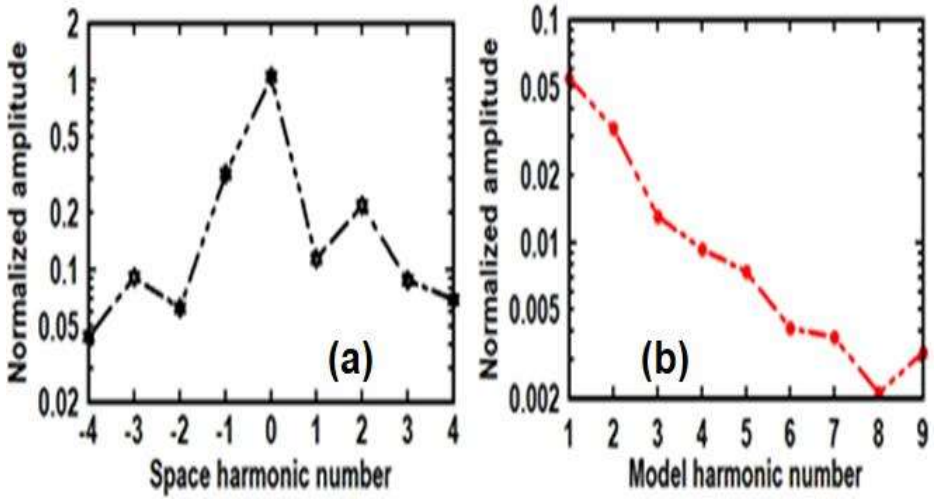

Figure 4. 2. (a) Normalized amplitude variation w.r.t. the space harmonics (b) Normalized amplitude variation w.r.t. the model harmonics

The beam wave synchronism required for effective energy transportation is defined by the dispersion diagram, shown in Figure4.3. The dispersion equation solution always gives the complex roots ($\tau_r + j\tau_i$), and therefore a discontinuity in the waveguide mode line near the cutoff is observed due to the attenuation caused by the dielectric loading. The intersection between the fundamental beam mode and the waveguide operating TE_{01} mode line occurs in the positive k_z region, which causes convective instability. The other backward wave parasitic modes, including TE_{11}, TE_{21}, TE_{02}, had negative k_z, which induces absolute instability, the PDL dielectric loading is the effective method to reduce this parasitic mode [161-163].

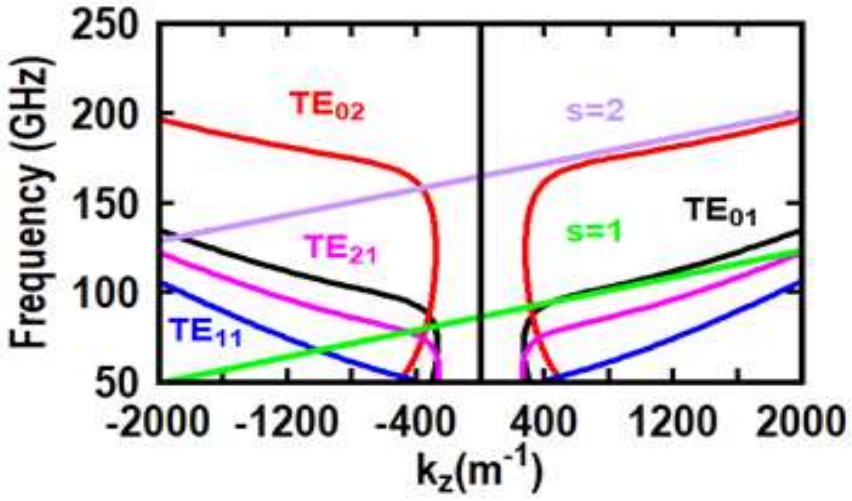

Figure 4. 3. Dispersion diagram of operating TE_{01} mode and different oscillation modes (TE11, TE_{21}, $TE0_2$)

The complexity of the interaction structure also depends upon the coupling factor of the operating mode and other parasitic modes with the energized gyrating beam. As shown in Figure4.4, the operating TE_{01} mode has an extreme coupling with the gyrating beam compared to the parasitic modes (TE_{02}, TE_{11}, TE_{21}) at r_b=0.45 r_w. The suppression of parasitic modes depends on the dielectric material property and

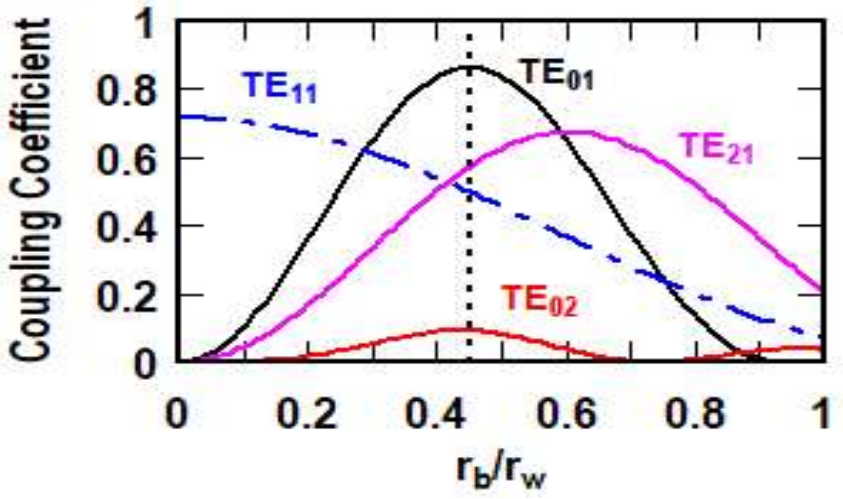

Figure 4. 4. coupling strength of different modes corresponding to the ratio of beam radius and waveguide radius.

thickness as observed in propagation constant expression [161],[165]

$$\tau_{\|}=\left[\left(\omega/c\right)^{2}-\left(x_{mn}/r_{w}\right)^{2}\left\{1-\left(1-j\right)T\left(1+\left(\frac{m^{2}\omega^{2}}{\omega_{c}^{2}\left(x_{mn}^{2}-m^{2}\right)}\right)\right)\right\}\right]^{1/2} \qquad [4.12]$$

Here δ is the skin depth, T is the thickness factor defined as:

$$\mathrm{T}=\left(\tan\left(\Delta r_{w}\left(1+j\right)/\delta\right)\right) \qquad [4.13]$$

The proper adjustment of the radial and axial dimensions of the dielectric loading material, Beryllium Oxide–Silicon Carbide (BeO-SiC), provides the freedom in controlling the instabilities. Figure4.5 shows the effects of dielectric slots on the attenuation of operating TE_{01} mode and parasitic modes, including TE_{02}, $TE_{21,\ and}$ TE_{11}. With the slot radius (Δr) of 0.5 mm and thickness of (w) 0.6 mm, the attenuation of TE_{11} oscillating mode is calculated as 16.84 dB /cm at 62.52 GHz, while TE_{02} and TE_{21} have 36 dB /cm at 167.42 GHz and 28.2 dB /cm at 73.5 GHz, respectively [Figure 4.5. (a)]. From Figure 4.5. (b) it is observed that the attenuation rate above the disc thickness of 0.6 mm is almost insensitive, which concludes that beam wave synchronism remains

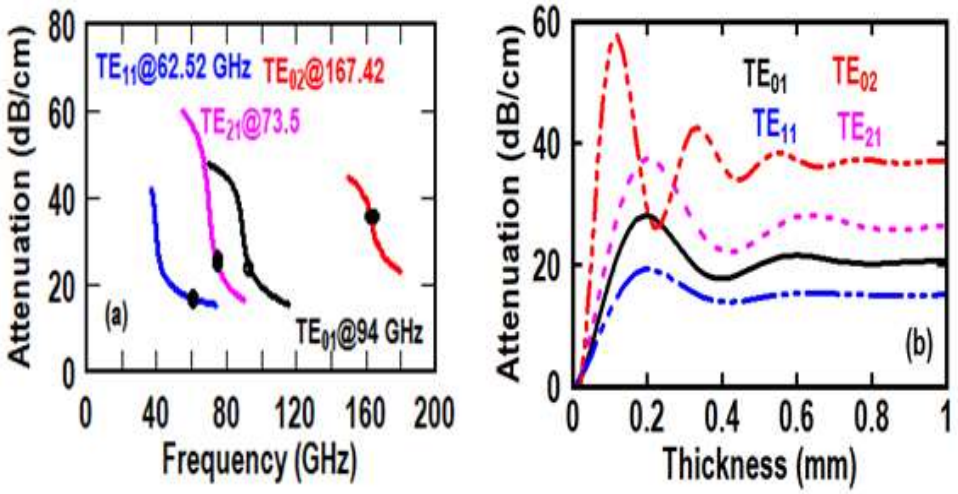

Figure 4. 5. (a) Attenuation rate Vs frequency for different modes and (b) change in attenuation rate Vs thickness of the dielectric material.

stable against the parameters variation. The PDL RF interaction structure has two regions: dielectric-loaded and copper regions. To restrain the instability issue keeping the waveguide length below the oscillation threshold limit. The critical length of each oscillating mode in the copper section is determined by using the linear theory [126], as a function of the beam current. As observed in Figure4.6, the SOL decreases in direct proportion to beam current, and the least SOL is observed corresponding to the TE_{02} mode for the beam current of 6 A In order to enhance the device output performance, the interaction length keeps large enough to avoid instability and provide the long beam wave interaction space. A dielectric-loaded section is introduced to increase the overall length of the interaction section [154]-[159],[161]-[165]. Figure4.7 shows the effect of the dielectric loading on SOL, and the least SOL is ~ 50 mm for the TE_{11}, which verifies that the lossy loading can increase the waveguide length limit compared to the unloaded waveguide. To avoid competitive mode, maintain the beam current below the start oscillation current [162]. Figure4.8 (a) shows the change in SOC as a function of pitch factor, corresponding to varied losses. It is observed that velocity ratio has a substantial impact on SOC since it raises electron transverse moment,

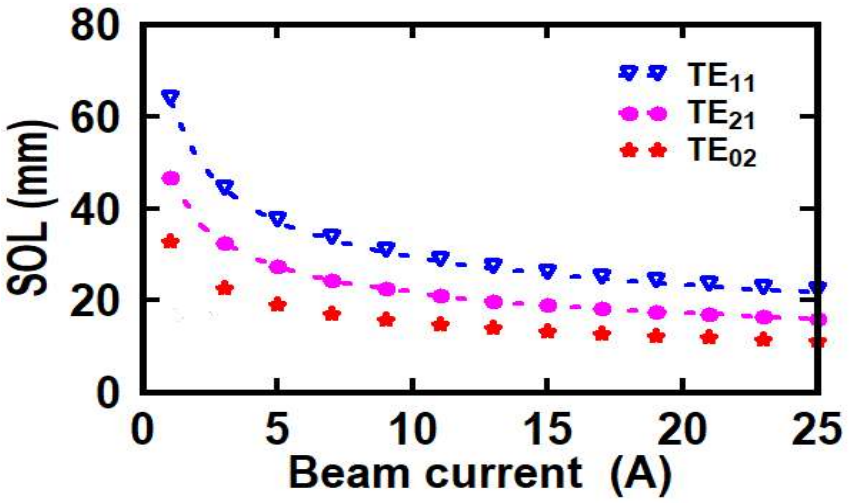

Figure 4. 6. SOL of different oscillating modes Vs beam current for unloaded structure.

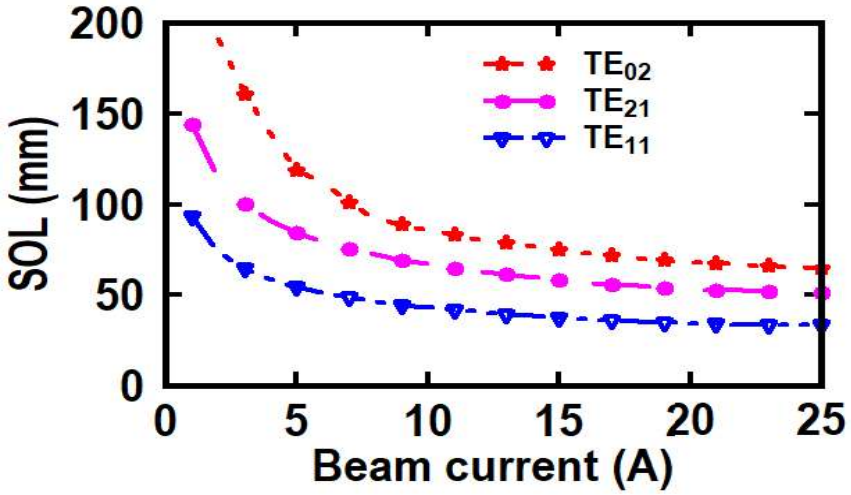

Figure 4. 7. SOL of different oscillating modes Vs beam current for loaded structure.

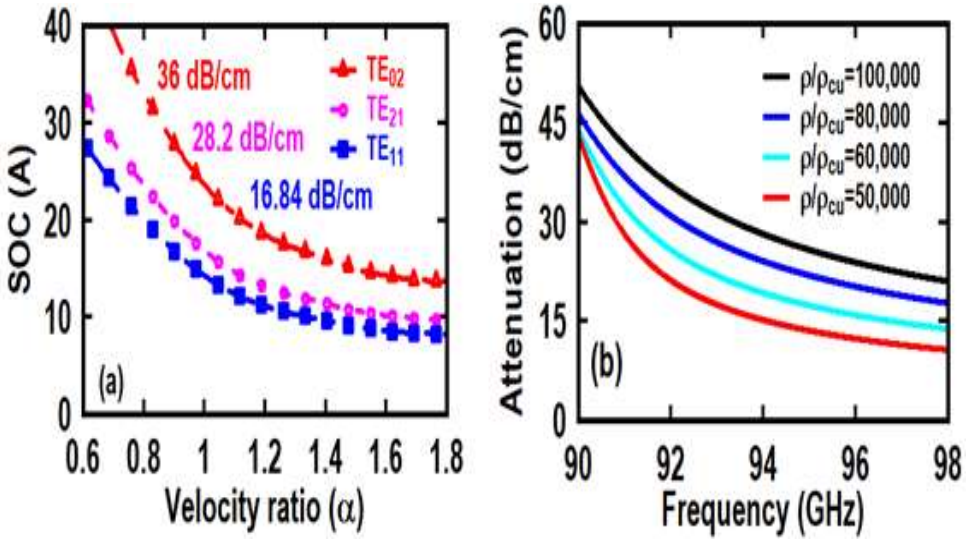

Figure 4. 8. (a) SOC Vs velocity ratio for different losses (b) Attenuation rate Vs frequency for different resistivity of the material.

which reduces SOC and also the SOC increases with the losses for specific value of velocity ratio. The resistivity of the lossy material, normalized to copper, provides an effective stabilization [90]. Figure4.8 (b) shows the attenuation change as a frequency function, corresponding to the different resistivity. The wall resistivity reduces the gain since it increases the attenuation. However, a longer lossy section can easily compensate this loss of gain.

The field development of desired TE_{01} and other spurious modes along the PDL waveguide is analyzed with the nonlinear, self-consistent, multimode theory [167]. Figure shows that the operating TE_{01} mode arises in the unloaded nonlinear RF circuit segment while other BWOs are suppressed due to the mode suppression property of the lossy dielectrics used in the RF section. These BWOs share only a small amount of power in the watt range, ensuring that the PDL waveguide clearly suppressed the second harmonic TE02 mode as well as the other competing modes, including TE_{11} and TE_{21}.

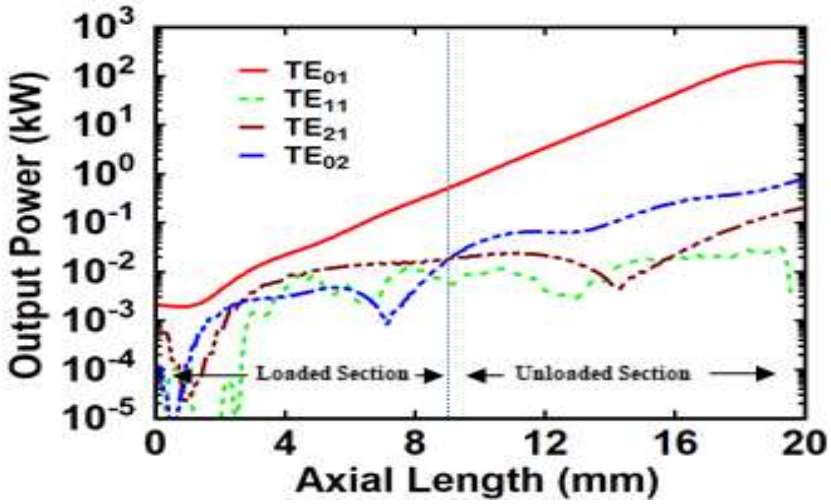

Figure 4. 9. RF output power growth along the axial direction of waveguide in various modes.

4.3. Modeling and PIC Simulation Study of PDL Gyro-Twystron Amplifier

Design and simulation of different sub-assemblies along with the interaction structure of fundamental harmonic W-band gyro-twystron with an output power of ~120kW, efficiency nearly ~34 % and saturated gain and 3 dB bandwidth of ~51dB and 2.2 GHz, respectively, is discussed in this section. A triode MIG has employed with beam voltage and current of 60 kV and 6 A, respectively, with the spread of ~ 2% and pitch factor of 1.6. A wave particle interaction system with periodic dielectric loading over the linear section (more practical case of dielectric loading) has been employed to

avoid the dielectric discharging problem. The electrostatic analysis of single stage depressed collector has done to further enhance the efficiency of the gyro-TWT. The EGUN beam optics code is used for the electrostatic simulation of electron beam in the collector region. Further, to extract the RF output for the wide band operation, a double disc RF window is designed. The detail design explanation of the different sections are given below.

4.3.1. Design of Magnetron Injection Gun (MIG)

Gyro amplifiers' maximum effective yielding depends on the quality of gyrating electron beam generated by the magnetron injection gun (MIG). There are two variants of MIG, (i) diode type MIG (single anode, compact and straightforward structure) and (ii) triode type MIG (double anode, complex structure, better parameters tuning options). The MIG schematic is shown in Figure 4.10, which is modelled by using the design parameters calculated through the available trade-off equations [50],[160].

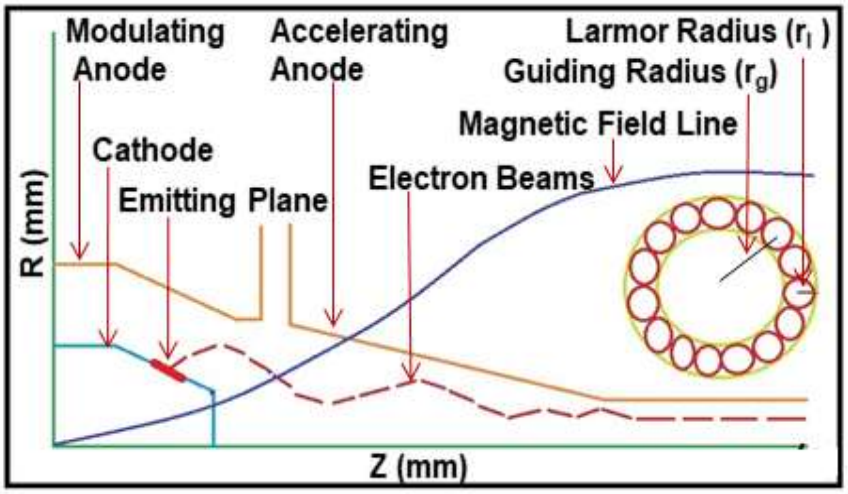

Figure 4. 10. Schematic of triode MIG geometry

For the optimum performance of the amplifier, the gyrating beams must have a large velocity ratio 1-2), lesser velocity spread, and an effective guiding beam radius [20]. The guiding centre radius is defined as $r_g = \left(r_b^2 - r_l^2\right)^{1/2}$ where r_b and r_l are the electron

beam radius and larmor radius, respectively. The guiding centre radius is used to fix the cathode radius as, $r_c^2 = F_m r_b^2$. $F_m = (B_o / B_c)$ is the magnetic compression ratio, where, B_o is the axial magnetic field and B_c is the field at the emitter.

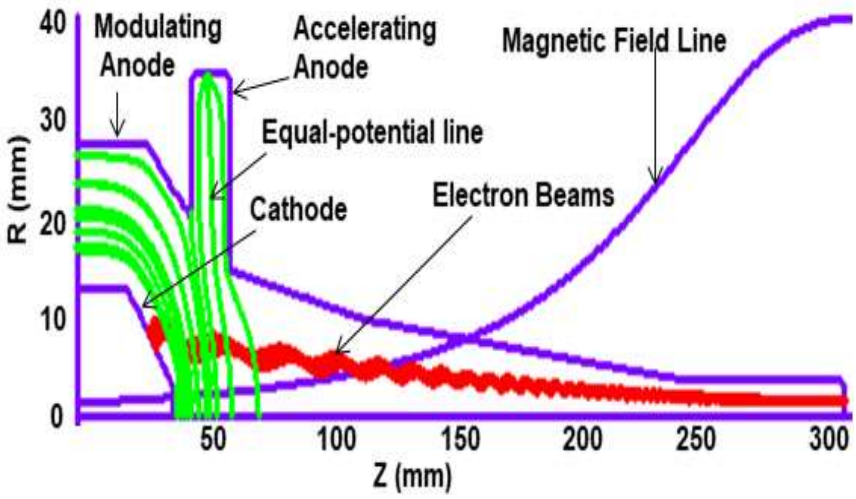

Figure 4. 11. Electron particles trajectory, and magnetic field profile of triode MIG using EGUN code.

The emitted electron beam quality depends on many factors like cathode angle, E- field at the emitter surface, applied voltage, current and the magnetic field near the emitting surface. The E field is linearly related with the voltage as,

$$E_c = \frac{(V_a / r_c)\cos\theta_c}{\ln(r_c + d_{ca}\cos\theta_c / r_c)} \qquad [4.14]$$

where, V_a, d_{ca} and θ_c are the anode voltage, cathode anode gap, and cathode angle, respectively. To obtain higher efficiency, the velocity ratio should be high enough, and the velocity spread as low as possible. The velocity ratio depends on the anode voltage and magnetic field, as shown below,

$$\alpha = \sqrt{F_m E_c^2 \sin^2\theta_c \Big/ \left(\left(1 - 1/\gamma_o\right) B^2 c^2 - F_m E_c^2 \sin^2\theta_c\right)}, \qquad [4.15]$$

where γ_o is the relativistic factor, and c is the speed of light. The present MIG [Figure 4.11] is designed using E-GUN code.

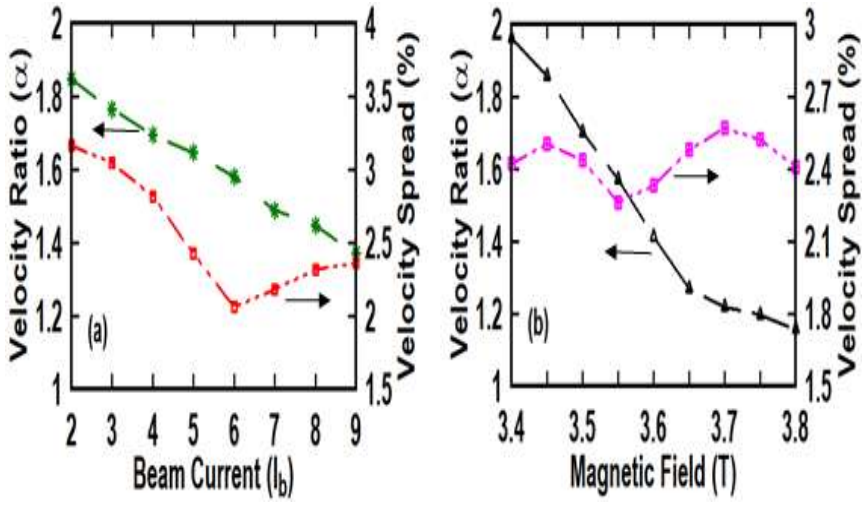

Figure 4. 12. (a) Change in beam velocity ratio and velocity spread variation with the (a) beam current and (b) magnetic field.

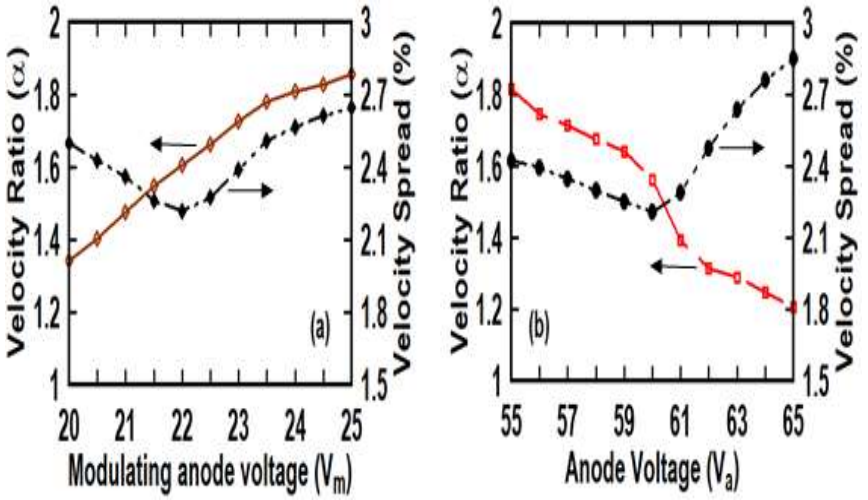

Figure 4. 13. Change in beam velocity ratio and velocity spread variation with the (a)modulating anode voltage and (b)anode voltage.

In Fig 4.12 (a), as the beam, current increases, the velocity ratio and spread start to fall because of the space charge effect, which alters the electric field near the cathode [160]. The velocity ratio decreases from 1.8 to 1.4 [Figure 4.12(b)], as the magnetic field is increased from 3.4 T to 3.8 T due to the variation in transverse velocity [160], while velocity spread varies from 2.2% to 2.6% [Figure12 (b)]. The optimization of modulating anode voltage and anode voltage to emit the electron beam with effective velocity ratio and spread is shown in Figure 4.13. Figure 4.13 (a) shows the continuous

rise in velocity ratio and variation in spread from 2.2 % to 2.6 % with the modulating anode voltage. The electric field near the cathode strongly depends on the anode voltage, causing the shift in velocity ratio and velocity spread [Figure 4.13 (b)]. The optimized electron beam parameters are shown in Table 4.1.

Table 4. 1. MIG PARAMETERS FOR W-BAND GYRO-TWYSTRON CIRCUIT DESIGN

Parameters	Value
Beam Voltage (V_b)	60 kV
Modulating Anode Voltage (V_m)	22 kV
Beam Current (I_b)	6 A
Pitch Factor (α)	1.6
Velocity Spread	2.2 %
Guiding radius (r_g)	0.92 mm
Cathode radius (r_c)	6.8 mm
Required Magnetic Field (B)	3.55 T
Cathode Angle (Φ)	52°
Compression ratio(f_m)	28
Emitter Strip length (L)	2.4 mm
Current Density (J_c)	7.4 A/cm^2

4.3.2. Cold Simulation Study of PDL Gyro-Twystron

The present gyro-twystron is shown in Figure4.15, and consists of three cavities in conjunction with an output waveguide, which are modeled independently to study their electromagnetic behavior. The input cavity is designed to provide the modulated electron beam, whose cutoff frequency remains lower than the desired operating frequency. The cavity radius is defined as, $r_{cav} = x_{mn} c / \omega_c$, where the x_{mn} is the eigenvalue of the operating TE_{mn} mode and ω_c is the angular cutoff frequency of the cavity. The cavity length is kept lower than the drift tube length in order to have sufficient energy for modulation to arise inside the cavity.

The Eigenmode solver in "CST Microwave Studio" [134] is used to explore the electromagnetic properties of the various cavities, including their operating mode,

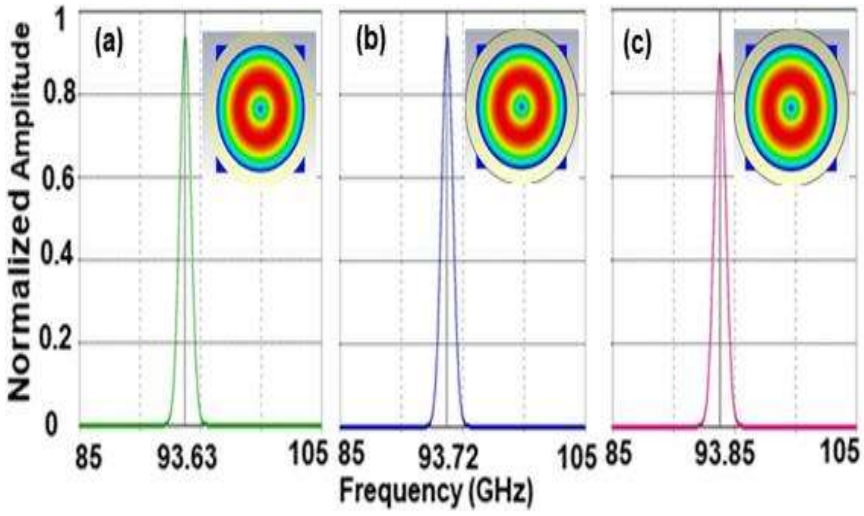

Figure 4. 14. Resonant frequency and corresponding contour plot of TE_{01} mode in (a) cavity I, (b) cavity II, (c) cavity III.

resonating frequency, and quality factor. The different cavitie's desired quality factors (Q1 = 126, Q2 = 110, and Q3 = 106) are achieved by filling them with dielectric Beryllium Oxide–Silicon Carbide (BeO-SiC) with the dielectric property of (ε_r = 11.52 − j 3.55). In a transient solver, the postprocessing is performed to observe the resonating frequency and operating modes of each cavities. Figure4.14 show that all cavities are operating in desired TE_{01} mode and resonating at different frequencies , ensuring that all cavities are stagger tuned. The drift tube's radius (r_d) is taken as it yields the field-free region, where the ballistic bunching arises and avoids the beam interception [104]. This radius follows the inequality $r_b < r_{dt} < r_{cut}$, where r_b is the gyrating beam radius. The drift tube's length is fixed to provide sufficient isolation between the cavities and calculated as, $L_{dt} > 4.6 \Big/ \sqrt{\left(x_{mn}/r_{dt}\right)^2 - \left(w_c/c\right)^2}$ [104]. The drift tube is loaded with a dielectric to avoid the interaction between the adjacent cavities.

4.3.3. Design of PDL RF Interaction Structure

In the design of PDL gyro-twystron, the primary concern is that the dielectric loading is essential for eliminating parasitic oscillations. The total length of the

waveguide and the type of dielectric material are chosen judiciously to damp the oscillations effectively. The waveguide section of 20 mm long and 2.05 mm radius are calculated and modelled with the copper. The BeO-SiC ($\varepsilon_r = 11.52 - j3.55$) dielectric ring with a radial thickness of 0.5 mm and an axial thickness of 0.6 mm is periodically inserted into the metal grooves as a lossy object, and the separation between the dielectric rings is fixed as 0.5 mm. The cold propagation behavior of the dielectric loaded waveguide offered an attenuation of 16.84 dB /cm, 28.2 dB /cm and 36 dB /cm attenuation for TE_{11}, TE_{21} and TE_{02} modes, respectively. The overall structural parameters of the device shown in Table 4.2.

Table 4. 2. DESIGN PARAMETERS FOR A PDL GYRO-TWYSTRON

Parameters	Value
Cavity Radius	1.989 mm
Cavity Length	4.5 mm
Drift Section Radius	1.989 mm
Drift Section Length	15 mm
Output Waveguide Radius	2.05 mm
Loaded Section Length	9 mm
Unloaded Section Length	11 mm
Total Waveguide Length	20 mm
Dielectric constant	11.52 – j3.55
Dielectric Ring radial Thickness	0.5 mm
Dielectric Ring Axial Thickness	0.6 mm

4.3.4. PIC Simulation Results and Validation

The present W-band gyro-twystron is modelled by using a 3D particle-in-cell (PIC) code “CST Particle Studio” [134], based on the finite integration technique (FIT). The PIC solver computes the beam wave interaction and update the field profile at small time interval using the leapfrog scheme. The time step in this self-consistent PIC simulation depends upon the mesh size, which leads to trade-off between simulation and

accuracy. The entire structure is divided into very small mesh cells for evaluating the device performance accurately with the hexahedral meshing technique. Here the ten cells per wavelength with the smallest and largest cell size of 0.03 and 0.3086, respectively. This mesh set generates total mesh cells of 2360155. The PIC simulation performed under the boundary condition of zero tangential electric field (E_t=0) at the waveguide surface. The beam wave interaction potency depends on the gyrating electron beam quality, a DC emission model is used to emit the gyrating electron beams with, beam voltage and current of 60 kV and 6 A, respectively, along with other beam parameters as decided in the design of MIG using E-Gun discussed in section 4.3.1.

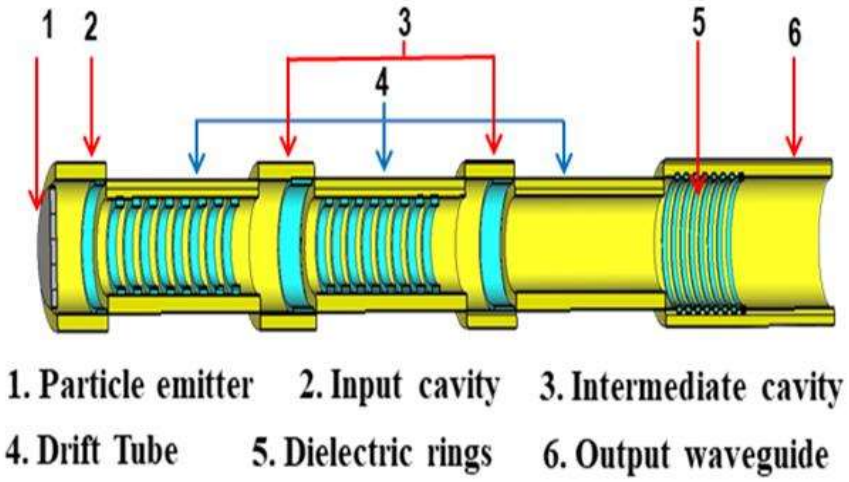

Figure 4. 15. CST modelling of dielectric loaded gyro-twystron.

An axial DC magnetic field of 3.65 T is applied throughout the structure to synchronize the gyrating beam and electromagnetic wave. The input signal is excited at port 1, which includes the desired operating mode. Further, the non-reflection boundary conditions were used at the output port of the interaction circuit. 24 modes are set at the output port to calculate the spurious oscillation of TE_{11}, $TE_{02,}$ and TE_{21} modes and the operating TE_{01} mode. When observing the spurious competing TE_{11}, TE_{21} and TE_{02} modes [Figure4.16 (a)], their amplitude is too small comparison to the operating mode

[Figure4.16 (b)]. This decreased amplitude of the competing mode demonstrates that the growth of the competing modes are successfully restricted within the loaded waveguide segment. In this continuous interaction process, the generated RF output is observed at the output port using the post-processing feature available in CST. The temporal amplification of the input power developed in the operating TE_{01} mode at the output port [Fig .4.17 (a)] predicted an instantaneous power of ~240 kW and the time average power of ~120kW with ~34% efficiency corresponding to 1W RF input power. The operating mode (TE_{01}) (inlet diagram) and the operating frequency (94 GHz) of the designed structure are verified with the Fourier of the output signal developed

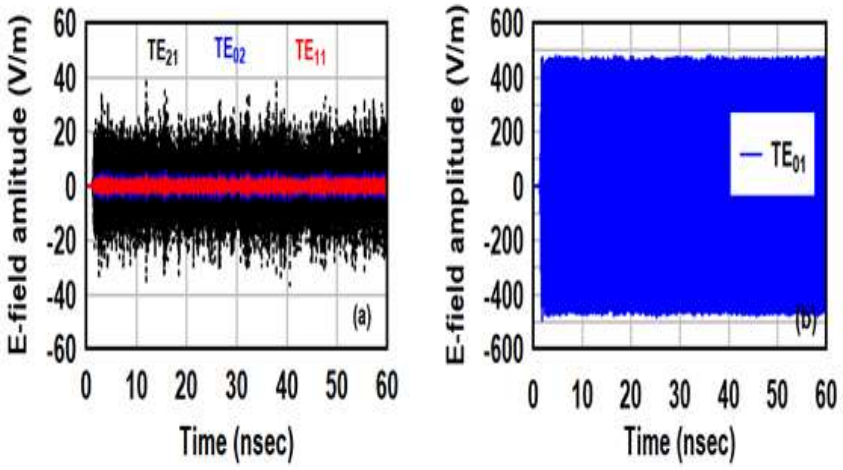

Figure 4. 16. (a) E-field amplitude of the different oscillating modes and (b) the operating mode at the output port.

[Figure4.17 (b)]. The designed amplifier's performance also depends on how efficiently the loaded material attenuates the oscillatory modes. The attenuation of material depends on its physical dimensions and dielectric property. Figure4.18 (a) shows the change in output power for the loading material's dimension and observed the maximum power of ~120 kW with a radial thickness of 0.5 mm and axial thickness of 0.6 mm. The variation in the RF output power with the frequency corresponding to different normalized resistivity is studied as shown in Figure 4.18 (b).

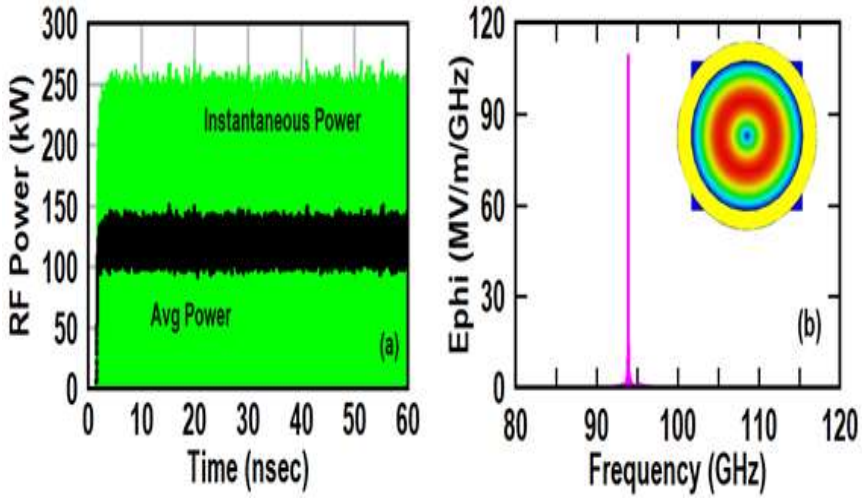

Figure 4. 17. (a) Temporal growth of the output signal developed in the operating mode and (b) operating frequency and mode (inlet) of the output signal at the output port.

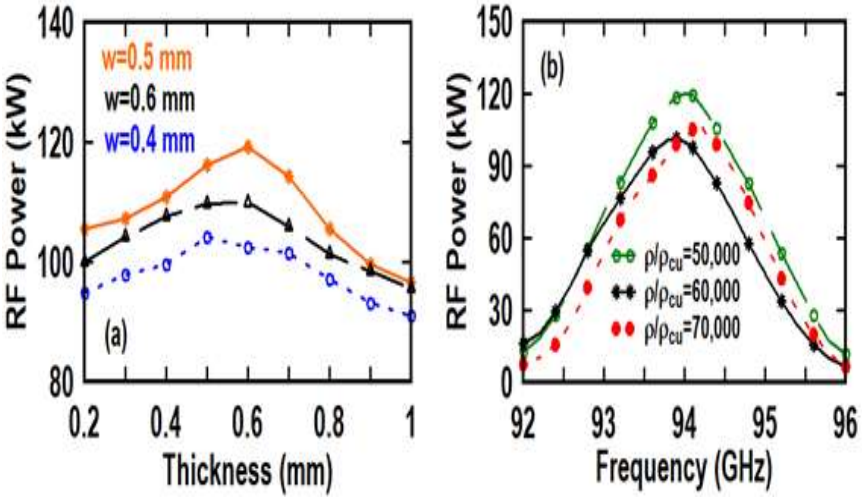

Figure 4. 18. Variation of RF power Vs (a) different radial thickness for various axial thickness and (b) frequency for different dielectric material resistivity.

As the resistivity increases, the peak RF power decreases, and a shift in the peak is observed. This change is due to an alteration in the attenuation rate. The spread in the electron velocity degrades the beam quality and deteriorates the device's output performance. The electron beam with zero spread has the best synchronism with the electromagnetic wave and transfers the energy efficiency, and as the spread increases, the output power and bandwidth are decreased [Figure 4.19 (a)]. The variation of the RF output power in the loaded amplifier is observed, as the RF

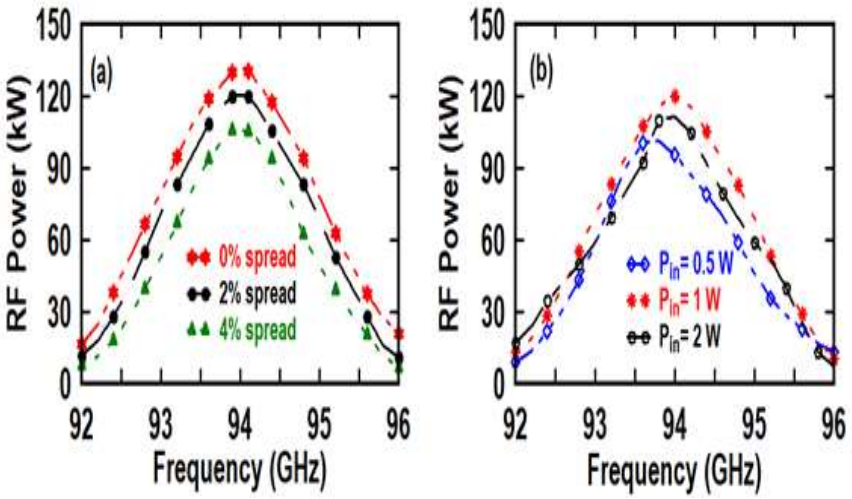

Figure 4. 19. Change in RF power Vs (a) frequency for different velocity spread and (b) frequency for different drive power.

drive is varied. Figure 4.19 (b) shows the maximum output power of 120 kW with the bandwidth of ~2.2 GHz corresponding to 1 W drive power. As the drive power is shifted back and forth from its optimized value, a fall-off is observed in the output power and bandwidth. The effect of drive power on the efficiency and gain of the amplifier is shown in Figure 4.20 (a). The maximum efficiency and gain are calculated as ~34% and ~51 dB, respectively with the beam parameter of 60 kV and 6 A.

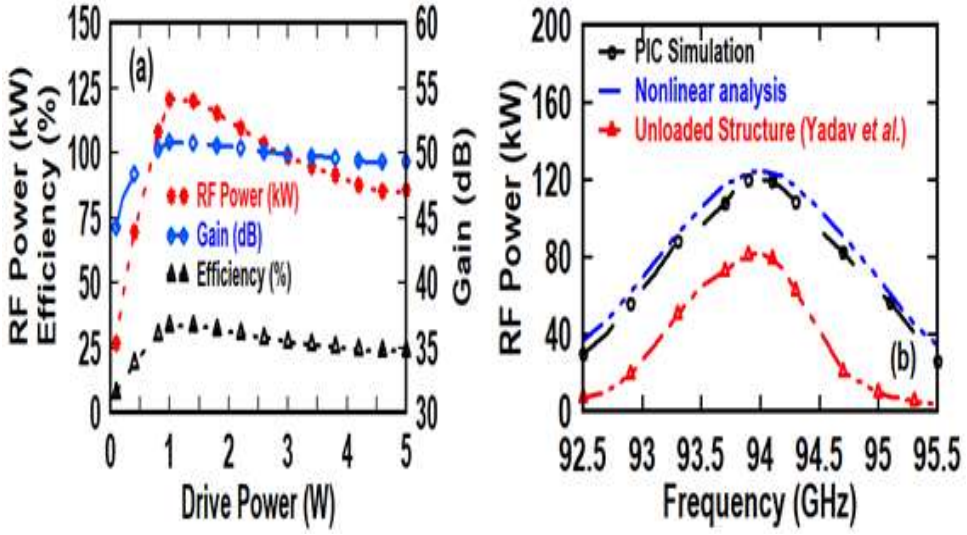

Figure 4. 20. (a) Change in RF power, efficiency and gain of the oprating mode with drive power and (b) comparison of RF power Vs frequency for the PDL and unloaded gyro-twystron.

The calculated output power of the present PDL gyro-twystron through PIC simulation is compared with the nonlinear theory [Figure 4.20 (b)], which shows a close agreement. It is observed that the performance of PDL gyro-twsytron shows a significant improvement in terms of RF output power and bandwidth, as compared to a unloaded gyro-twystron [169].

4.4. Design of Output Systems

4.4.1. Design of Single Stage Depressed Collector

The spent electrons beam exiting out from the waveguide section still contains a significant amount of energy. This substantial amount of energy is released in a single-stage depressed (SSD) collector that is held at a depressed potential (V_{dep}). The depressed potential is optimized to decelerate the gyrating beams sufficiently. These decelerating electron beams travel under the decreasing magnetic field and transform their orbital energy into axial energy [26]. The trajectory of the spent electrons beam in SSD collector is traced with E-GUN code under the optimized magnetic field, as shown in Figure 4.21. The quality of the designed SSD collector is described by collector efficiency (η_c), which depends upon the depressed potential [26] as, $\eta_c = V_{dep}/V_b(1-\eta_{RF})$,

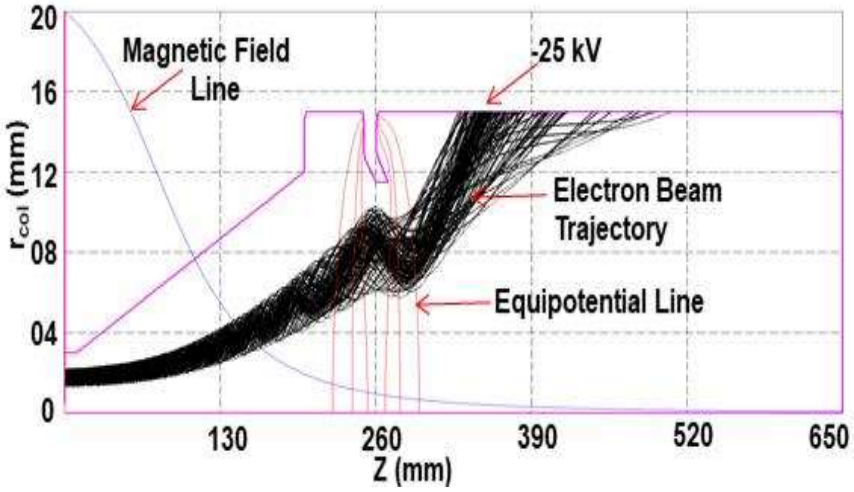

Figure 4. 21. 2D design of SSD collector showing the particle trajectory and magnetic field profile.

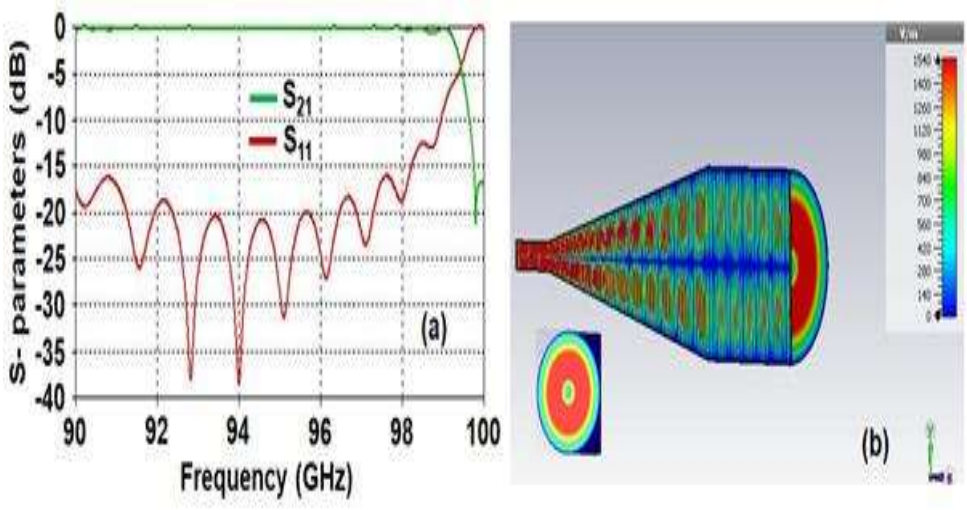

Figure 4. 22. (a) S-parameter and (b) electric field pattern of TE_{01} mode in SSD collector.

where η_{RF}, V_{dep}, V_b are the device RF efficiency, depressed voltage and beam voltage, respectively. With the optimized depressed voltage (V_d) of -25 kV, about 62 % of the energy present in the spent electrons beam has recovered in designed SSD collector. This recovered energy significantly enhanced the overall efficiency $\eta_T = \eta_{RF} / \left(1 - V_{dep}/V_b\right)$ at the high V_{dep} with the constant V_b. The optimized SSD collector with 62 % collection efficiency raises the device's overall efficiency from ~34 % to ~57 %. The propagation characteristic of the collector region is analyzed because some portion of the electron beam may be reflected into the RF interaction region and causes oscillations in the device. Also, mode conversion may occur in the collector region. Therefore, the collector region must have high transmission and low reflection characteristics. The transmission and reflection performance of the SSD collector was observed through the cold simulation in "CST Microwave Studio", as shown in the Figure 4.22. The reflection (S_{11}) and transmission (S_{21}) parameters of the SSD collector [Figure4.22 (a)] shows that S_{21} is maximum as ~0.001 dB and S_{11} is minimum as ~ -38 dB at the operating frequency, *i.e.*, 94 GHz. The electric field distribution of TE_{01} mode is

preserved without any mode conversion at the output port of the SSD collector, as shown in Figure 4.22 (b).

4.4.2. Design of Double Disc RF Output Window

The RF window is an essential sub-assembly which isolates the vacuum environment inside the waveguide from the external atmosphere. The window dimensions and material properties are chosen as it provides minimum return loss and insertion loss as well as effective power handling capacity and enough mechanical strength [26]. For a wide bandwidth requirement, an effective matching is obtained through a double disk window. The internal reflection should be minimum and defined as [52]

$$|\Gamma| = 2\left|\frac{\sin x(a^2-1)\left\{(a+1)^2\cos(x+y)-(1-a)^2\cos(x-y)\right\}}{\left\{(a+1)^2-(1-a)^2e^{i2x}\right\}^2-\left\{(1-a^2)(1-e^{i2x})\right\}^2e^{i2y}}\right| \qquad [4.16]$$

where, x and y depends on the disk thickness and the separation between the disk, a is the normalized axial wavenumber. The total reflection should be at the minimum value if the separation between the disks follows the condition,

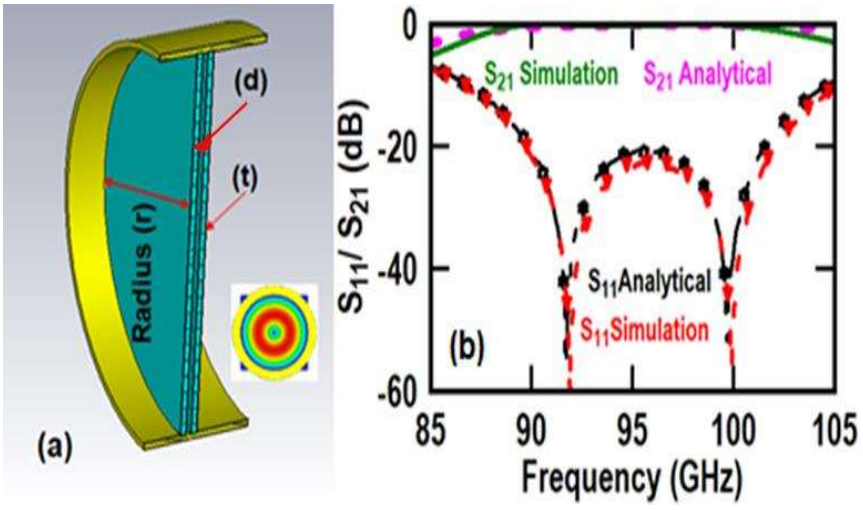

Figure 4. 23. Double disc RF window (a) CST model and (b) its propagation behavior.

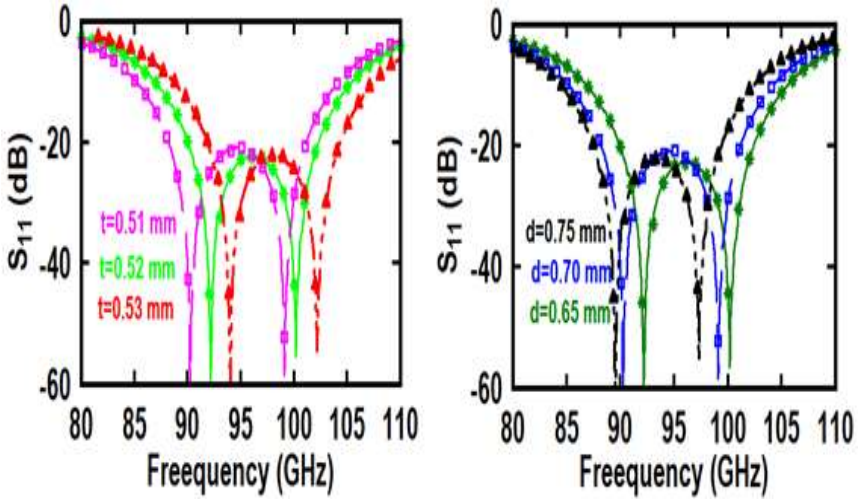

Figure 4. 24. Change in reflection coefficient (S11) (a) for different disc thickness and (b) for the change in disc separation.

$\left[\cos\left(x_o + y_o\right)/\cos\left(x_o - y_o\right)\right] = \left[\left(1-a\right)/\left(1+a\right)\right]^2$, where, x_o and y_o are the integer multiple of π. During vacuum sealing process it is difficult to maintain the disc separation accurately as it has very less contact area to braze with the structure [170]. Therefore, discs are inserted into copper structure in depth of 0.2mm to maintain the disc separation during vacuum sealing process. The designed double disk window is shown in Figure 4.23 (a). The reflection coefficient of the designed window is calculated using the simulation and the available theory. The reflection coefficient is below -20 dB for the frequency range from 92 GHz to 100 GHz, corresponding to a disk radius (r) of 15 mm [Figure 4.23 (b)]. The operating bandwidth of ~8 GHz is observed corresponds to the optimized window thickness (t) and the separation (d) of 0.52 mm and 0.7 mm, respectively. The window dimensions are optimized within the acceptable compromise in bandwidth and the disk strength. Figure 4.24 shows the sensitivity of the disk thickness [Figure 4.24 (a)] and the separation [Figure 4.24 (b)] on the operating bandwidth from the centre frequency. The sensitivity analysis shows that the operating bandwidth of ~8 GHz corresponds to the optimized window thickness (t) and the separation (d) of 0.52 mm and 0.7 mm, respectively.

4.5. Conclusion

In this chapter, an all-metal structure, namely, a circular waveguide loaded with thin annular discs has been analysed in the fast-wave regime, in view of the potential application of the structure to attenuate the spurious oscillating modes TE_{11}, TE_{02}, TE_{21} and widening the bandwidth of stagger tuned gyro-twystron. The dispersion relation, as special cases, has passed on to that of a smooth-wall circular waveguide and to that findings of the present chapter certainly suggest the use of a PDL as an additional parameter for controlling the dispersion of a disc-loaded waveguide.

The influence of circuit and electrical design parameters over the performance of PDL gyro-twystron operating in TE_{01} mode at fundamental harmonic has been extensively studied through the simulation investigation. The outcome of this study is as discussed below:

- The PIC simulation of the stagger tuned PDL gyro-twystron operating at 94 GHz is predicted the RF output power of 120kW kW with the gain of 51 dB. The electronic efficiency and 3 dB bandwidth are 34 % and 2.2 GHz, respectively.
- A triode type MIG is designed using 2D EGUN code for the generation of the gyrating electron beam of 60 kV and 6A by considering ~2% spread and pitch factor of 1.6. Also, The use of SSD collector has improved the device efficiency from ~34 % to ~57 %. The double disc RF output window provide the 8 GHz operating bandwidth.
- The present PDL gyro-twystron has shown a substantial improvement in the output power (~120 kW), gain (~51 dB) and bandwidth (~2.2 GHz), as compared to an unloaded gyro-twystron.

- The current gyro-twystron employs a shorter lossy section with a stagger tuned cavities and gyrating beam of larger velocity ratio (>1.5) and gives the following advantages as compared to gyro-TWT such as:
  (i) Shorter RF interaction circuit length as well as overall device length makes gyro-twystron not only the compact device but also the cost-effective.
  (ii) Preserve the high efficiency with high stable output power. Therefore, it is hoped that the present PDL based W-band gyro-twystron would be a potential amplifier for millimeter wave radars.